Role of Air–Sea Interaction in the Long Persistence of El Niño–Induced North Indian Ocean Warming*

YAN DU

Key Laboratory of Tropical Marine Environmental Dynamics, South China Sea Institute of Oceanology, Chinese Academy of Sciences, Guangzhou, China, and International Pacific Research Center, University of Hawaii at Manoa, Honolulu, Hawaii

SHANG-PING XIE

International Pacific Research Center, and Department of Meteorology, University of Hawaii at Manoa, Honolulu, Hawaii

GANG HUANG AND KAIMING HU

Institute of Atmospheric Physics, Chinese Academy of Science, Beijing, China

(Manuscript received 16 April 2008, in final form 21 August 2008)

ABSTRACT

El Niño induces a basin-wide increase in tropical Indian Ocean (TIO) sea surface temperature (SST) with a lag of one season. The north IO (NIO), in particular, displays a peculiar double-peak warming with the second peak larger in magnitude and persisting well through the summer. Motivated by recent studies suggesting the importance of the TIO warming for the Northwest Pacific and East Asian summer monsoons, the present study investigates the mechanisms for the second peak of the NIO warming using observations and general circulation models. This analysis reveals that internal air–sea interaction within the TIO is key to sustaining the TIO warming through summer. During El Niño, anticyclonic wind curl anomalies force a downwelling Rossby wave in the south TIO through Walker circulation adjustments, causing a sustained SST warming in the tropical southwest IO (SWIO) where the mean thermocline is shallow. During the spring and early summer following El Niño, this SWIO warming sustains an antisymmetric pattern of atmospheric anomalies with northeasterly (northwesterly) wind anomalies north (south) of the equator. Over the NIO as the mean winds turn into southwesterly in May, the northeasterly anomalies force the second SST peak that persists through summer by reducing the wind speed and surface evaporation. Atmospheric general circulation model experiments show that the antisymmetric atmospheric pattern is a response to the TIO warming, suggestive of their mutual interaction. Thus, ocean dynamics and Rossby waves in particular are important for the warming not only locally in SWIO but also on the basin-scale north of the equator, a result with important implications for climate predictability and prediction.

1. Introduction

El Niño–Southern Oscillation (ENSO) is a mode of air–sea interaction in the equatorial Pacific with profound influences on the global climate. For example, El Niño causes sea surface temperature (SST) to increase over the tropical Indian Ocean (TIO) with a one-season lag (Klein et al. 1999; Lau and Nath 2000, 2003; Alexander et al. 2002). This basin-wide warming pattern is so robust that it is detected from sparse ship observations in an early study of Weare (1979). It emerges as the first empirical orthogonal function (EOF) mode of IO SST variability, with nearly uniform warming over the entire basin as well as the South China Sea (SCS) and Indonesian seas (Fig. 1). This mode is referred as the Indian Ocean Basin mode (IOBM; Yang et al. 2007). The IOBM is highly correlated with the Niño-3.4 SST index, at 0.91 with a 5-month lag. The second EOF mode represents the Indian Ocean dipole (IOD), with a weak

* International Pacific Research Center Publication Number 558 and School of Ocean and Earth Science and Technology Publication Number 7576.

Corresponding author address: Yan Du, Key Laboratory of Tropical Marine Environmental Dynamics, South China Sea Institute of Oceanology, Chinese Academy of Sciences, 164 West Xingang Rd., Guangzhou 510301, China.
E-mail: duyan@scsio.ac.cn

DOI: 10.1175/2008JCLI2590.1

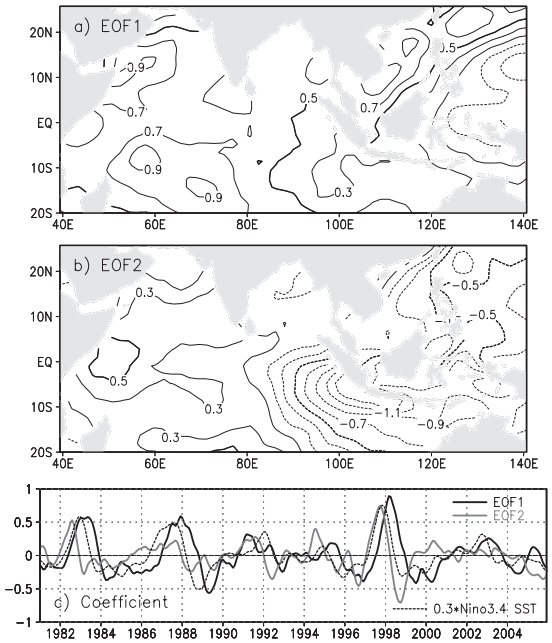

FIG. 1. (a) First and (b) second Indian Ocean SST EOF modes, and (c) their principal components (PCs) smoothed with a 7-point running mean. In (a) and (b), first contours are ±0.1°C at 0.2°C intervals. The ±0.5°C contours are highlighted in thick lines. ERSST SST is used and filtered with a 4–84-month bandpass filter. EOF1 and EOF2 explain 20% and 16% of the total variance in the first 10 modes, respectively. PC1 correlates with the Niño-3.4 (5°S–5°N, 170°–120°W) SST at 0.91 with a 5-month lag while EOF2 is at 0.70 with a 3-month lead.

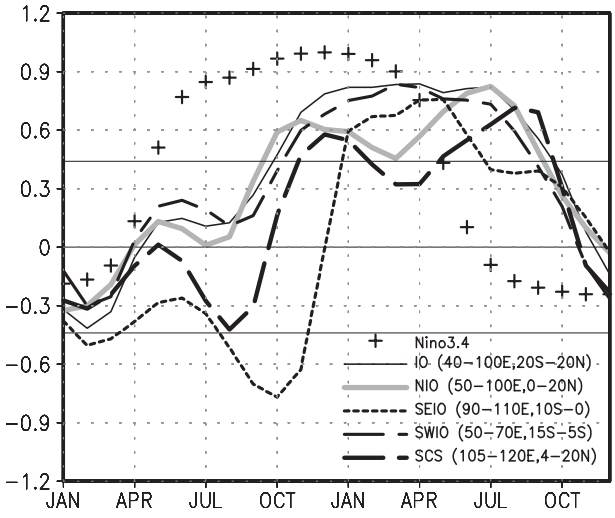

FIG. 2. Correlation of Indian Ocean SST with the NDJ(0) Niño-3.4 SST index. The domains of SEIO and SWIO are consistent with previous studies (Saji et al. 1999; Xie et al. 2002) to identify typical ocean processes. Two straight lines show the 95% confidence level.

warming over the western IO and a major cooling in the east off Java and Sumatra (Saji et al. 1999; Webster et al. 1999). The IOD involves ocean dynamical adjustments indicative of the Bjerknes feedback. For a more complete discussion of modes of IO variability on intraseasonal to interdecadal time scales, we refer to a recent review by Schott et al. (2009). In addition, Yamagata et al. (2004) is a review focusing on IOD, Annamalai and Murtugudde (2004) focus on the IO's influences on the Asian monsoon, and Chang et al. (2006) focus on the role of ocean dynamics in IO climate variability.

The IOBM is the focus of this paper. Specifically, we are interested in what sustains the TIO warming for nearly a year. Figure 2 shows the correlation and regression of TIO SST referenced to the Niño-3.4 SST index from November(0) to January(1) [NDJ(0)]. Here, numerals "0" and "1" denote the developing and decay years of El Niño, respectively. While Niño-3.4 SST decays rapidly in April–June(1), the TIO warming persists 4–6 months longer and decays in August–September(1). Recent studies indicate that the IOBM is not just simply a passive response to ENSO but acts like a capacitor. ENSO excites the IOBM like a battery charging a capacitor, but the IOBM can exert its climatic influence like a discharging capacitor (Yang et al. 2007; Xie et al. 2009). Indeed, TIO SST anomalies may affect the amplitude (Yu et al. 2005; Wu and Kirtman 2004; Dommenget et al. 2006), and development (Annamalai et al. 2005a) and termination (Kug and Kang 2006) of ENSO. The TIO warming contributes to the formation of an anomalous anticyclone in the lower troposphere over the Northwest (NW) Pacific during the El Niño decay (Watanabe and Jin 2002) and to the delayed onset of the Indian summer monsoon (Annamalai et al. 2005b). In the ensuing summer with ENSO SST having dissipated in the equatorial Pacific, the persistent TIO warming forces the anomalous anticyclone over the subtropical NW Pacific (Yang et al. 2007; Xie et al. 2009).

Surface heat flux is an important mechanism for the TIO warming. In particular, ENSO-induced changes in atmospheric circulation reduce cloud cover and evaporation, initiating the warming over much of the TIO Basin (Klein et al. 1999; Alexander et al. 2002; Lau and Nath 2003; Tokinaga and Tanimoto 2004). The tropical southwest IO (SWIO) is an exception where ocean Rossby waves are important for the warming (Xie et al. 2002; Huang and Kinter 2002). During the mature phase of El Niño, changes in the atmospheric Walker circulation produce anticyclonic wind anomalies over the south IO, forcing a downwelling Rossby wave in the ocean (Masumoto and Meyers 1998; Yu et al. 2005). The Rossby wave deepens the thermocline and raises SST as it propagates into the SWIO where the mean thermocline is shallow (Xie et al. 2002). While the SWIO warming may sound as independent of that over the rest of the

TIO domain, our analysis shows that the former sustains the latter during the decay phase of El Niño.

While the initiation of the IOBM has been studied extensively, little is known about the mechanism for its long persistence. This becomes an important issue in light of the TIO capacitor effect to prolong ENSO's influences through June–August [JJA(1); Xie et al. 2009]. Illustrating the richness and complexity of the TIO warming, the SST increase displays a peculiar, second peak over the north IO (NIO) and SCS during JJA(1) when El Niño has dissipated (Fig. 2). It is unclear what maintains the large-scale changes in atmospheric circulation that lead to the secondary summer peak over the NIO and SCS.

The NIO warming weakens between the winter and summer peaks during March–May (1) [MAM(1)] when an antisymmetrical pattern develops in the atmosphere. Precipitation increases (decreases) with northwesterly (northeasterly) wind anomalies south (north) of the equator (Kawamura et al. 2001; Xie et al. 2002; Wu et al. 2008). Kawamura et al. (2001) suggest that this antisymmetrical atmospheric pattern is due to a positive wind–evaporation–SST (WES) feedback. Indeed the trade winds prevail on either side of the equator during winter and early spring, meeting a necessary condition for the WES feedback (Xie and Philander 1994). Coupled general circulation model (GCM) results of Wu et al. (2008) indicate that this antisymmetric mode may arise from air–sea interaction within the TIO, with ENSO teleconnection often triggering its formation. The role of ocean dynamics in the spring formation of the TIO antisymmetric mode is unclear from these studies. The possibility that the Rossby wave–induced SWIO warming anchors the antisymmetric mode is hinted by results from an atmospheric GCM coupled with a slab mixed layer model over the TIO and forced by observed SST over the tropical eastern Pacific. Lacking ocean Rossby wave dynamics, the model fails to reproduce the south TIO warming and the antisymmetric wind pattern in the spring following El Niño (Figs. 3 and 4 of Lau and Nath 2003). The wind biases conceivably affect subsequent evolution of TIO SST anomalies via the surface flux.

The present study investigates ocean–atmospheric processes that give rise to the long persistence of the TIO warming induced by El Niño, using observational diagnosis and ocean–atmospheric models. The mechanism for the second summer peak in the NIO/SCS warming is our major focus. Our results show that the SWIO Rossby wave forces the antisymmetric wind pattern during spring. This antisymmetric pattern, the anomalous northeasterlies north of the equator specifically, initiates the second warming over the NIO by reducing evaporation as the climatological winds turn westerly in May. Thus, the second summer warming results from internal IO–atmosphere interaction.

The rest of the paper is organized as follows. Section 2 describes data, the method, and an atmospheric GCM. Section 3 analyzes the mixed layer heat budget and investigates the mechanisms for the SST warming in various TIO subdomains. Section 4 explores the role of air–sea interaction in the NIO warming. Atmospheric GCM experiments support the hypothesis that the SWIO Rossby wave anchors both the spring antisymmetric mode and the second warming peak in summer. Section 5 explores other possible mechanisms for TIO warming, and presents an individual warming case. Section 6 is a summary.

2 Data and model

a. Data

The National Centers for Environmental Prediction–Department of Energy (NCEP–DOE) monthly mean reanalysis (Kanamitsu et al. 2002) is used, including SST, 10-m wind, surface latent heat flux, specific humidity, and air temperature. The time period spans from January 1979 to December 2007. Surface solar radiation is derived from the satellite-based International Satellite Cloud Climatology Project (ISCCP), from July 1983 to December 2004 (Schiffer and Rossow 1985). The Climate Prediction Center (CPC) Merged Analysis of Precipitation (CMAP) provides monthly rain rate, from January 1979 to November 2007 (Xie and Arkin 1997).

Ocean temperature, sea surface height (SSH), and mixed layer depth are obtained from the ocean GCM for the Earth Simulator (OFES; Masumoto et al. 2004; Sasaki et al. 2008) hindcast, which is forced by the NCEP–National Center for Atmospheric Research (NCAR) daily reanalysis from January 1950 to December 2003. The model resolution is $0.1° \times 0.1°$ with 54 vertical levels. Vertical resolution varies from 5 to 15 m in the upper 200-m layer. We analyze the output from January 1979 to December 2003. A comparison with satellite altimeter observations shows a good agreement in phase with the OFES hindcast of SSH variability. The amplitude tends to be slightly weak in the hindcast.

The IO displays large intraseasonal (Han et al. 2007) and interdecadal (Deser et al. 2004) variability. For the latter, in particular, there is a steady warming trend in SST since the 1950s (e.g., Du and Xie 2008). A 4–84-months bandpassing filter is applied to extract interannual anomalies. For surface heat flux, downward flux that warms the ocean is defined as positive.

Our presentation centers on regression and correlation analyses referenced to the Niño-3.4 SST index averaged during NDJ(0). Typical decorrelation time for the

bandpass-filtered time series is slightly less than 1.5 yr (Fig. 2). For a time series from 1979 to 2007 (for SST and precipitation), we estimate that the degree of freedom is 18, excluding the first and last year due to the sidelobe effect of the filter. Based on t test, the 95% confidence level corresponds to a correlation coefficient of 0.44.

b. Latent heat flux decomposition

Latent heat flux (LHF) variations involve changes in both atmospheric conditions—such as wind speed—and SST. The bulk formulas for LHF can be expressed as

$$Q_E = \rho_a L C_E W[q_s(T) - \mathrm{RH} q_s(T - \Delta T)], \qquad (1)$$

where ρ_a is surface air density, L is the latent heat of evaporation, C_E is the transfer coefficient, W is the surface wind speed, RH is the relative humidity, ΔT is the sea minus air temperature difference, and $q_s(T)$ is the saturated specific humidity following the Clausius–Clapeyron equation.

LHF is often regarded as a simple damping in mixed layer budget analyses but instead consists of distinct atmospheric forcing and oceanic response. The oceanic response arises from the SST dependence of evaporation and may be cast as a Newtonian cooling term by linearizing the above bulk formula

$$Q'_{\mathrm{EO}} = \overline{Q_E} \beta T', \qquad (2)$$

where the overbar and prime denote the mean and perturbation, respectively, and $\beta = 1/q_s\,(dq_s/dT)$. The residual $Q'_{\mathrm{EA}} = Q'_E - Q'_{\mathrm{EO}}$ may be regarded as atmospheric forcing due mostly to changes in wind speed, relative humidity, and air–sea temperature difference. Similar decomposition methods have been used elsewhere to study the atmospheric forcing of SST changes via latent heat flux (de Szoeke et al. 2007; Du and Xie 2008).

c. Atmospheric GCM

To study processes of IO–atmosphere interaction, we use an atmospheric GCM, ECHAM version 5 developed at the Max Planck Institute for Meteorology in Hamburg, based on the European Centre for Medium-Range Weather Forecasts (ECMWF) model (Roeckner et al. 2003). The ECHAM5 employs a spectral dynamic core and utilizes a semi-implicit leapfrog time-differencing scheme. We use a version with triangular truncation at zonal wavenumber 63 (T63; equivalent to 1.9° horizontal resolution) and 19 sigma levels in the vertical.

The model is forced with the observed monthly climatology of SST and sea ice. We analyze a 20-yr period of the control (CTL) simulation. We carry out three experiments. In the TIO run, we add 1°C SST over the TIO (20°S–20°N, 40°–110°E). In the other two experiments, the same SST anomalies are imposed in the south TIO (SIO; 20°S–0°, 40°–110°E) and SWIO (20°S–0°, 40°–80°E), respectively. In all three experiments, the SST anomalies are kept constant in time and the model is integrated for 20 yr. Thus, the experiments are equivalent to 20-member ensemble runs.

3. Regional characteristics of the warming

Figure 3 shows the SST regression, zonally averaged in 40°–100°E, upon the NDJ(0) Niño-3.4 SST index. Typical regression coefficient is 0.2°–0.3°C, corresponding to 0.3°–0.45°C in amplitude. The TIO warming first takes place off the equator in September–October(0), centered at 10°N and 20°S (Fig. 3a). It persists for nearly a year until July–August(1). Based on evolution characteristics, the TIO warming may be divided into three distinct parts: the NIO, off-equatorial (0°–15°S) and subtropical (15°–30°S) south Indian Ocean (SIO). The SIO is further divided into west and east basins where SST anomalies display different phases (Fig. 2). We will return to this point in the next section.

The NIO warming is characterized by the double peaks in October–November(0) and JJA(1), respectively. In general regional SST anomalies over the TIO correlate well with the atmospheric forcing component of LHF (AtF-L), with the latter leading by 1–2 months (Fig. 3b). The off-equatorial SIO is an exception, where ocean dynamics and cloud–radiative forcing are important. In the subtropical SIO, an anticyclone develops in the east during the mature phase of El Niño, and the associated anomalous westerlies weaken the prevailing southeast trades, giving rise to a strong warming that spans from October(0) to May(1) (Behera and Yamagata 2001; Xie et al. 2002; Chiodi and Harrison 2007). Forced by observed SST over the tropical eastern Pacific, an atmospheric GCM coupled with a slab mixed layer model over the TIO captures this warming in the subtropical but not the tropical SIO (Alexander et al. 2002; Lau and Nath 2003).

a. North Indian Ocean and South China Sea

Over the NIO, the AtF-L displays two peaks nearly coincident with the SST warming, both associated with easterly wind anomalies (Fig. 3b). Figure 4 shows the zonal structure of this double-peaked warming over the NIO and SCS. Again, the AtF-L is overall well correlated with the SST anomalies, with a 1–2-month lead. The September–November [SON(0)] warming is mostly confined to the Arabian Sea where the northeasterlies weaken the mean southwesterlies (Lau and Nath 2000).

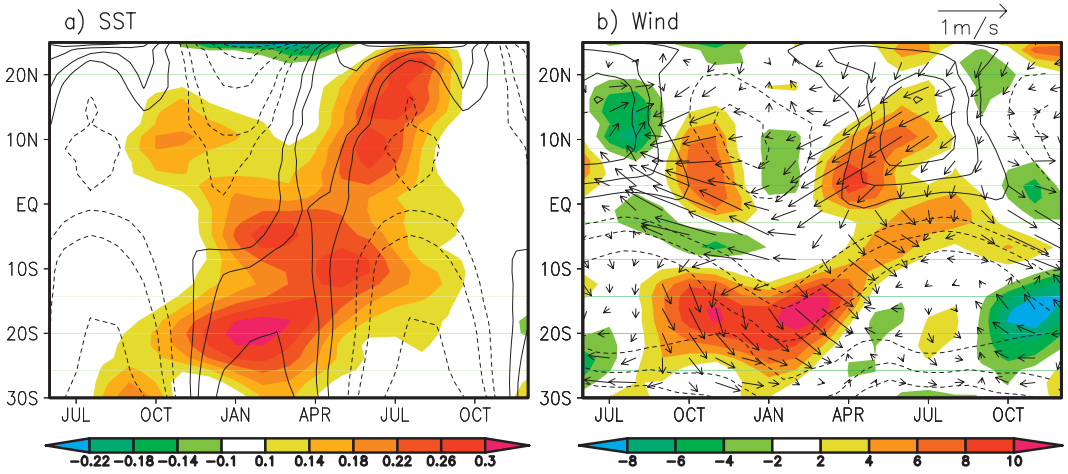

FIG. 3. Regression (shade) of (a) SST (°C) and (b) AtF-L (W m^{-2}), averaged zonally in 40°–100°E, upon the NDJ(0) Niño-3.4 index as a function of calendar month and lat. Seasonal variations expressed as deviations from the annual mean are superimposed in black contours: (a) SST (only ±0.5°C, ±1°C, and ±2°C contours) and (b) zonal wind velocity [contour intervals (CIs) at 2 m s^{-1}, with the zero contour omitted].

A weak AtF-L cooling follows, with the easterly anomalies intensifying the northeast monsoon. As the climatological wind turns westerly in April–May(1), the AtF-L becomes positive with anomalous easterlies, giving rise to the second warming in JJA(1) from the Arabian Sea to the Bay of Bengal.

The SCS warming also features two peaks in December(0) and August(1), respectively. They both lag those of the NIO warming by 1–2 months. Chen et al. (2007) note this apparent eastward propagation of SST warming. We suggest this phase lag of the SCS summer warming is related with the delayed onset of the climatological westerlies there. The monsoon westerlies first appear over the NIO and then progress eastward through the SCS into the NW Pacific (Fig. 4b). Positive AtF-L is associated with the mean westerlies as anomalous easterlies persist north of the equator from April(1). For the same reason, AtF-L and SST warming shows an apparent northward propagation over the NIO as the mean westerlies first appear on the equator in April and then in the NIO in May (Fig. 3). Eastern equatorial Pacific SST anomalies begin dissipating rapidly in April(1) (Fig. 2) and cannot be the direct cause of the NIO warming thereafter. Section 4 discusses what sustains easterly wind anomalies from the NIO to the NW Pacific.

b. Heat budget terms

This subsection examines important terms in the mixed layer budget over the TIO and its subdomains, including

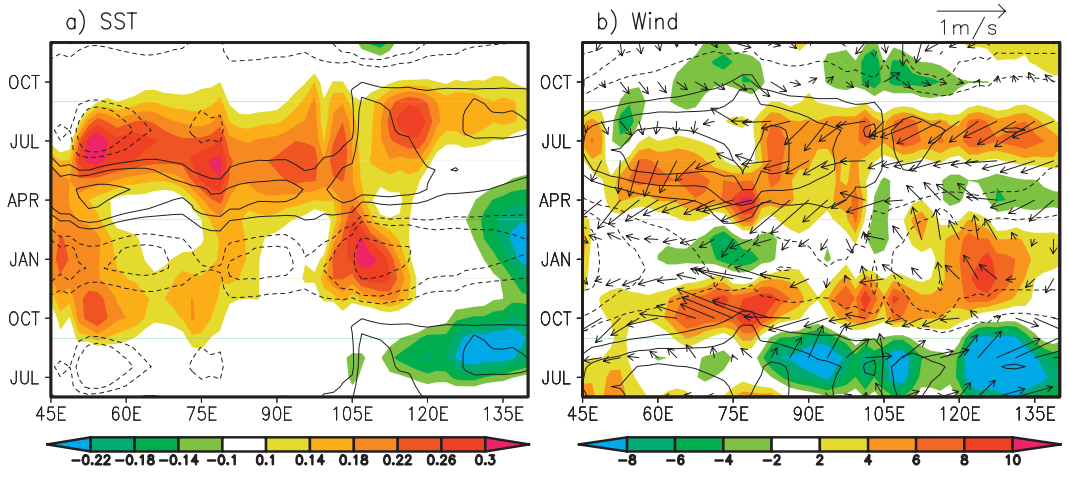

FIG. 4. As in Fig. 3, but for lon–time sections, averaged in 0°–20°N.

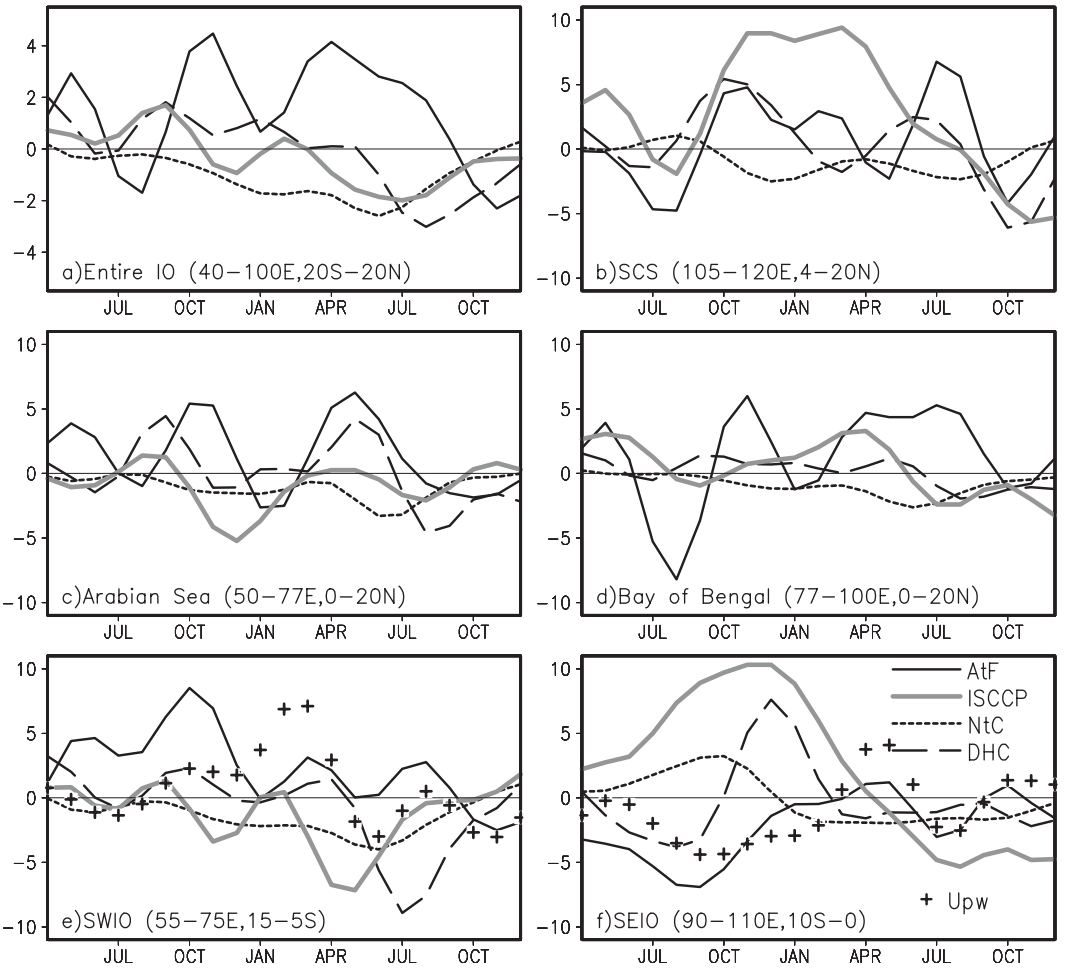

FIG. 5. Major terms of the mixed layer heat budget (W m^{-2}) in several regions, expressed as regression upon the NDJ(0) Niño-3.4 index. In (e) and (f), the regression of vertical heat advection at the 50-m level is shown by the plus signs. Abbreviations: AtF [atmospheric forcing component of latent heat flux (LHF)] solar (solar radiation from ISCCP), DHC (tendency of the mixed-layer heat content), and NtC (Newtonian cooling component of LHF).

AtF-L. We express them as their regression coefficients upon the NDJ(0) Niño-3.4 SST index (Fig. 5). For reference, the tendency of the mixed layer heat content (DHC) is calculated from DHC = $d(T\rho_s C_{ps} h_m)'/dt$, where ρ_s is seawater density, C_{ps} is the specific heat, and h_m is the mixed layer depth. DHC does not differ much from the SST tendency (not shown), with some difference in amplitude in the SIO, where the mixed layer entrainment/detrainment is important off Java and Sumatra in July–October(0) and over the SWIO thermocline dome. North of the equator, mixed layer depth variations have little influence on SST.

Averaged over the TIO, the AtF-L is the dominant mechanism for the warming (Fig. 5a), with two peaks in November(0) and April(1), respectively. It overcomes the Newtonian cooling and sustains the SST warming to JJA(1). Solar radiation contributes to the warming during July–November(0), consistent with Klein et al. (1999).

On the subbasin scale, relative contributions from these terms vary. North of the equator, the double-peak feature is very pronounced in AtF-L and DHC from the Arabian Sea to SCS (Figs. 5c,d,b). Solar radiation acts to reduce SST warming in the Arabian Sea during October(0)–March(1) (Fig. 5c) but contributes positively to the second warming during MAM(1) in the Bay of Bengal (Fig. 5d). It is very important for the SCS warming during September(0)–May(1) (Fig. 5b; Wang et al. 2006). Ocean dynamical processes contribute to the SCS warming, too: the reduced southward advection of cold water by the western boundary current in the southern basin during winter (Liu et al. 2004), and the weakened offshore development of upwelling filaments off Vietnam during summer (Xie et al. 2003).

South of the equator, the heat budget is quite different between the east and west basins. In the southeast TIO (Fig. 5f), SST warming is the latest of the entire basin in onset and does not start until December(0). Prior to this, negative SST anomalies develop in response to the upwelling off Java and Sumatra during July(0)–March(1) associated with occasional IOD occurrence (Saji et al. 1999; Murtugudde et al. 2000). The atmospheric forcing component of LHF contributes to the surface cooling as the southeasterly alongshore winds intensify (Tokinaga and Tanimoto 2004; Shinoda et al. 2004; Du et al. 2008). The SST cooling suppresses atmospheric deep convection and reduces cloud cover (Webster et al. 1999; Yu and Rienecker 1999; Klein et al. 1999). Enhanced solar radiation is a strong damping for the southeast TIO cooling during the IOD season [July–November(0)], much larger than the Newtonian damping due to the SST dependence of evaporation. The increased solar radiation contributes to the rapid warming over the southeast TIO from October(0) to January(1), so do changes in AtF-L and upwelling (Shinoda et al. 2004; Tokinaga and Tanimoto 2004).

c. Southwest Indian Ocean

Klein et al. (1999) report that surface heat flux does not explain the SST warming in the SWIO, where later studies show the importance of ocean downwelling Rossby waves (Xie et al. 2002; Huang and Kinter 2002), a conclusion supported by ocean model simulations (Murtugudde et al. 2000; Behera et al. 2000). Figure 5e shows the heat budget terms in our analysis over this region. The AtF-L is strong and positive during the El Niño developing phase,[1] with a peak in October(0). Solar radiation is almost always negative, especially during February–June(1) as a result of enhanced atmospheric convection. Vertical advection across the bottom of the mixed layer, diagnosed from the OFES hindcast, contributes strongly to the SWIO warming during January–April(1) when the ocean downwelling Rossby wave propagates through this region of the thermocline dome (Fig. 6a). The ocean advection turns weakly negative from May(1) as local Ekman pumping becomes upward from April(1) (Fig. 6a) in response to increased atmospheric convection. Thermocline depth anomalies begin to weaken but remain positive at least through July(1).

Near the El Niño mature phase [September–December(0)], strong downward Ekman pumping appears in the southeast TIO (Fig. 6a), associated with easterly wind anomalies near the equator (Fig. 3b). The equatorial easterly anomalies are due to ENSO teleconnection (Alexander et al. 2002; Lau and Nath 2003) and/or IOD (Rao and Behera 2005; Yu et al. 2005). The negative wind curls force a downwelling Rossby wave that propagates westward. The downwelling wind curls weaken from January(1) but persist until March(1), indicating a continuous influence of ENSO from the Pacific (Fig. 2).

SST warming shows a copropagation with the oceanic Rossby wave (Fig. 6b, shade; Xie et al. 2002), a tendency especially pronounced during March–July(1). SST anomalies continue to grow during April–May(1) when SSH anomalies of the Rossby wave already begin to decay. The annual Rossby wave that shoals the thermocline in SWIO during this period (Fig. 6b, contours; Périgaud and Delecluse 1992; Wang et al. 2001; Yokoi et al. 2008) may enhance the thermocline feedback, leading to the continued development of the SST anomalies.

Figure 7 shows the vertical structure of the downwelling Rossby wave in the OFES hindcast. Large temperature anomalies are found in a layer between the 20° and 24°C isotherms, with a maximum of 1.5°C, much larger than the SST anomalies. At the mature phase of El Niño [October–December OND(0)], Ekman downwelling deepens both the mixed layer and thermocline. On its way to the west, temperature anomalies rise from 80 m at 80°E in OND(0) to 60 m at 65°E in MAM(1), following the tilted thermocline (Fig. 7). During MAM(1), subsurface warming clearly reaches the sea surface, (Fig. 7b), indicative of thermocline feedback. By JJA(1), the thermocline anomalies and their surface signature are both weak (Fig. 7c). The upper-westward propagation of subsurface warming is captured following the 2006 El Niño by the newly complete Argo float array (Chowdary et al. 2009).

With ENSO decaying during February–June(1), the Rossby wave–induced warming over SWIO begins to exert its atmospheric influence.[2] Indeed, precipitation increases over SWIO during this period (Fig. 9; Xie et al. 2002). Cyclonic wind curls associated with intensified atmospheric convection act as a negative feedback and cause the downwelling Rossby wave to decay from March to April(1). SSH anomalies nearly disappear by September(1).

[1] This difference from Klein et al.'s analysis may be because of the use of different datasets: they use the Comprehensive Ocean–Atmosphere Data Set (COADS), and we use the NCEP–NCAR reanalysis. Ship observations are sparse in SWIO.

[2] Prior to this, the zonal precipitation dipole is associated with the IOD during September–November(0), and the continued reduction in rainfall in the southeast TIO until February(1) is due to the El Niño–induced subsidence.

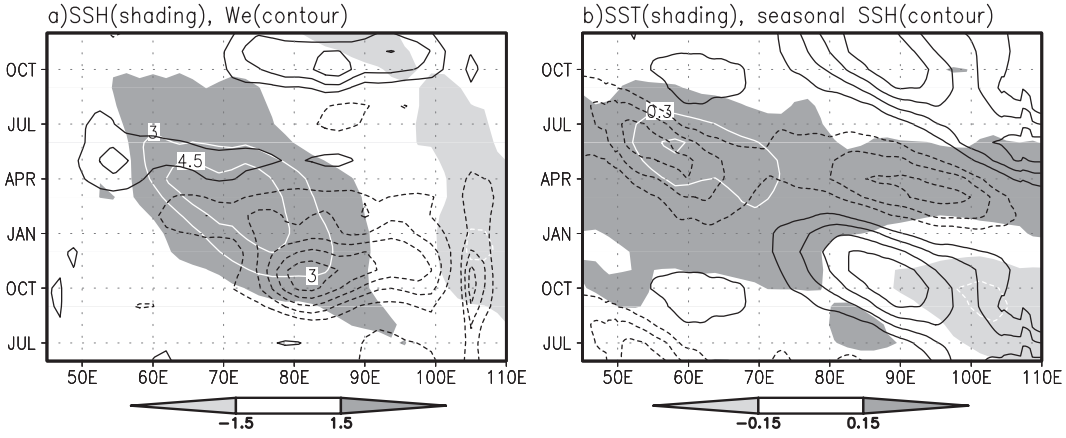

FIG. 6. Longitude–time sections of (a) SSH (shade with white contour lines, CIs at 1.5 cm), and (b) SST (shade with white contour lines, CIs at 0.15°C), averaged meridionally in 5°–15°S, expressed as regression upon the NDJ(0) Niño-3.4 index. Superimposed are (a) Ekman pumping (black contours at CI of 1 m month^{-1}), and (b) satellite SSH climatology (CI: 2 cm), with the zero contour omitted and negative values dashed.

4. Second NIO warming: Role of air–sea interaction

The SST warming peaks for the second time during JJA(1) over the NIO and SCS. Since the El Niño begins to decay from April(1), it must be something else that sustains the second warming over NIO and SCS. This section presents observational and modeling evidence that the Rossby wave–induced warming over the SWIO induces the second TIO and SCS warming by initiating a series of air–sea interaction.

a. Role of an antisymmetric atmospheric pattern during March–June(1)

The left panels in Fig. 8 show anomalies of SST, surface wind velocity, solar radiation, and AtF-L during March–April(1). Over the TIO, changes in solar radiation are mostly due to those in convective clouds, negatively correlated with rainfall anomalies (not shown). As ENSO begins to decay and its direct effect on the TIO weakens, atmospheric effects of TIO SST anomalies begin to emerge. The SWIO warming, in particular, intensifies atmospheric convection (Figs. 8g and 9). Convection weakens north of the equator, especially over the eastern TIO, SCS, and the NW Pacific. Consistent with the SST warming and intensified convection over the SWIO, surface wind anomalies feature a C-shaped, antisymmetric pattern, with northeasterlies north and northwesterlies south of the equator. The C-shaped wind pattern is a result of the Coriolis force acting on the northerly cross-equatorial winds to induce an easterly (westerly) component north (south) of the equator. Over the subtropical SIO, the anomalous northwesterlies weaken the prevailing southeasterly trades, helping to maintain the SST warming (Fig. 8d). Over the equatorial NIO, the mean winds turn westerly during March–April (Fig. 10a), and the northeasterly anomalies act to warm the ocean. Farther to the north in the subtropical NIO, wind anomalies are weak, and so is AtF-L.

During May–June(1), atmospheric anomalies remain largely unchanged and are antisymmetric about the equator, but AtF-L turns positive over the NIO as the southwest monsoon begins (Figs. 8b,e and 10b). Rainfall and wind anomalies are weaker over the SCS and NW Pacific than during March–April(1). The northeasterly anomalies occupy the entire NIO, reducing the prevailing southwest monsoon and inducing a strong warming effect via AtF-L.

Kawamura et al. (2001) first notice the antisymmetric pattern of atmospheric anomalies during spring following El Niño and suggest that they result from the WES feedback between the TIO and atmosphere (see also Wu et al. 2008). The WES feedback favors an antisymmetric mode of ocean–atmospheric anomalies under prevailing easterlies on either side of the equator (Xie and Philander 1994). This condition for WES feedback is met over the TIO during winter and early spring. Over the NIO, the WES mode, especially its northeasterly anomalies, probably contributes to the reduction of the SST warming during early spring.

Kawamura et al. (2001) and Wu et al. (2008) both stress the WES feedback, but they differ in how the antisymmetric pattern is initiated. Kawamura et al. (2001) suggest that asymmetric heating over the western Pacific in response to ENSO triggers the westward-propagating WES mode. Wu et al. (2008) point to the SWIO SST warming but attribute it to heat flux changes induced by anticyclonic winds in the tropical Indian Ocean.

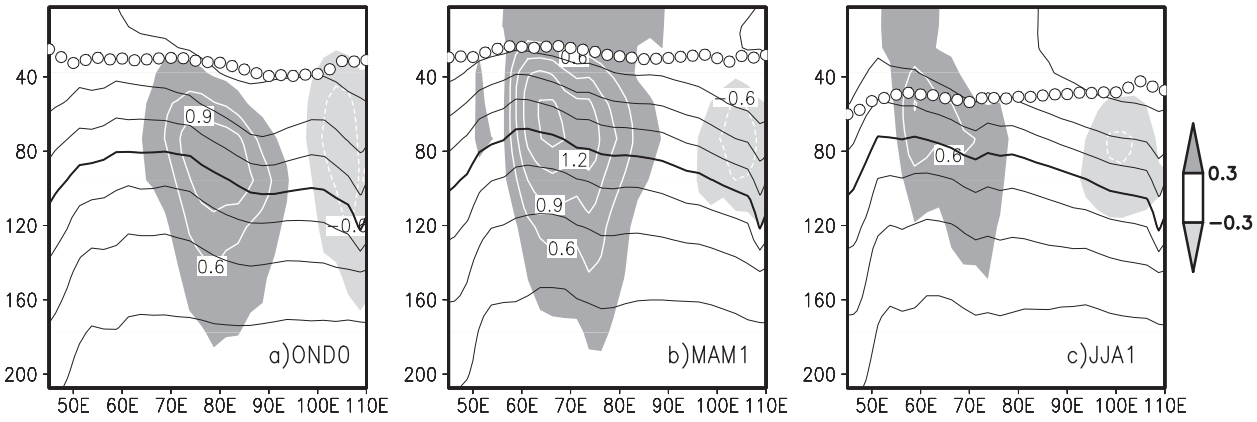

FIG. 7. Regression (shade with white contour lines, CIs at 0.3°C) of OFES temperature anomalies, averaged meridionally in 5°–15°S, upon the NDJ(0) Niño-3.4 index (over 95% confidence level) superimposed on the climatology of temperature (black contours at CI of 2°C; the 20°C contours thickened) and the mixed layer depth (open circle).

While these studies focus on the WES feedback and the development of cross-equatorial SST gradients during February–April(1), ours emphasizes the subsequent development and shows that the antisymmetric wind pattern is anchored by the ocean Rossby wave, and induces the second NIO warming in summer.

b. *Model experiments*

This subsection presents results from atmospheric GCM experiments demonstrating that during spring and early summer, the antisymmetric pattern of atmospheric anomalies is forced by positive SST anomalies over the

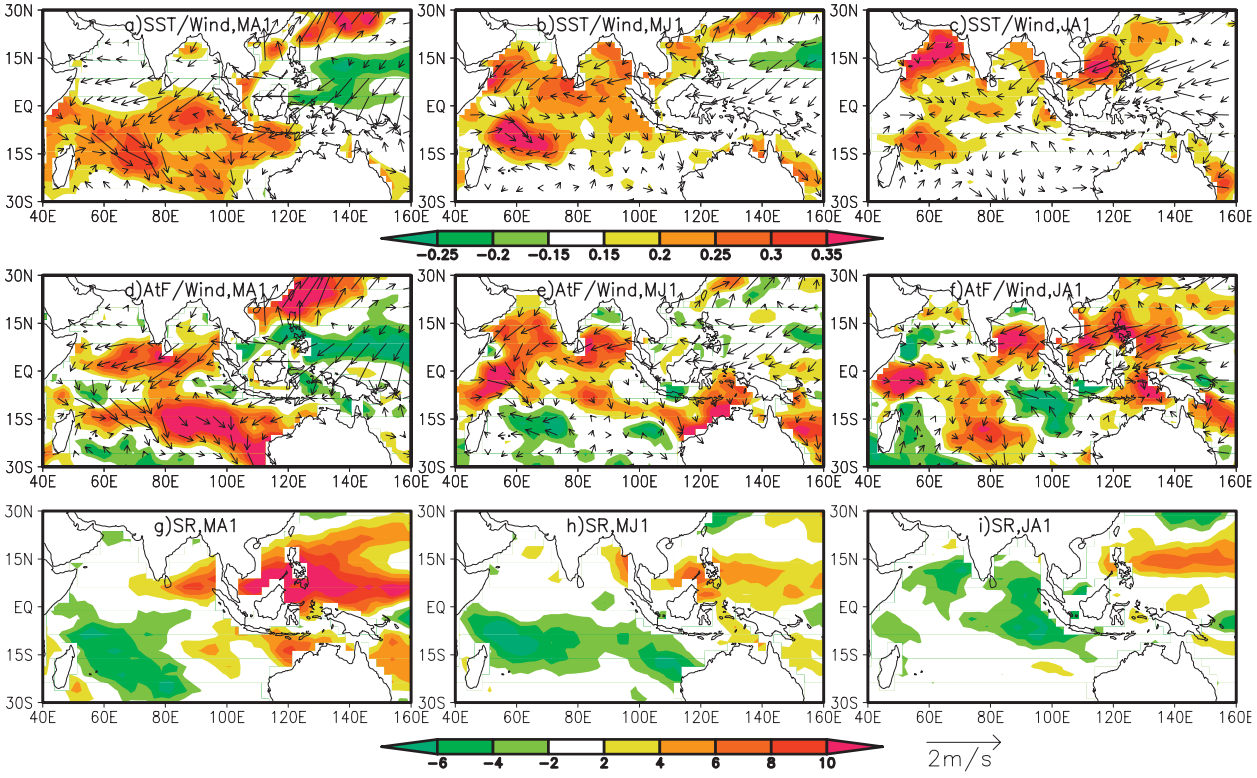

FIG. 8. SST (°C), wind velocity (m s^{-1}), and heat flux (W m^{-2}) anomalies expressed in regression upon the NDJ(0) Niño-3.4 index during (left) March–April(1), (middle) May–June(1), and (right) July–August(1). AtF stands for the atmospheric forcing component of latent heat flux, SR is the solar radiation from ISCCP.

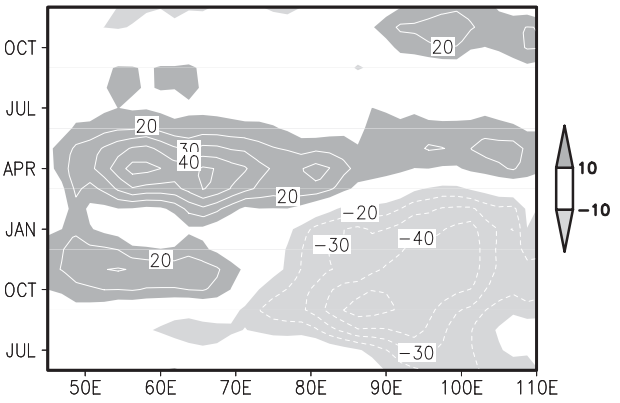

FIG. 9. Regression of CAMP precipitation (mm month^{-1}) upon the NDJ(0) Niño-3.4 index: averaged in 5°–15°S in a longitude–time section.

SIO, which in turn are maintained by the downwelling ocean Rossby waves. This conclusion is consistent with the persistence of this atmospheric anomaly pattern from March(1) to June(1) (Fig. 8), during which SST anomalies in the eastern equatorial Pacific rapidly decay. While Kawamura et al. (2001) and Wu et al. (2008) emphasize the cooling effect of northeasterly wind anomalies during the northeast monsoon season, the same wind anomalies turn into a warming effect as the southwest monsoon takes over in the NIO, giving rise to the second peak of the SST warming.

We conduct four atmospheric GCM integrations. In the control run, the model is forced by the observed monthly climatology of SST. A 1°C SST anomaly over the TIO, SIO, and SWIO is imposed uniformly in the TIO, SIO, and SWIO runs, respectively. Anomalies averaged for 20 yr are presented here, equivalent to results from 20-member ensembles. We have conducted experiments with more realistic SST anomalies of 0.5°C and obtained qualitatively very similar results. We also have conducted 1°C cooling experiment over TIO. With the sign difference, the response to a 1°C TIO cooling yields similar results to the response to a 1°C warming, except that the former are somewhat weaker than the latter, especially over the Arabian Sea.

The TIO run reproduces the antisymmetric pattern of atmospheric anomalies observed during March–April(1). Rainfall increases over the SWIO and decreases over the eastern NIO, SCS, and NW Pacific (Fig. 11a). The remote response over the SCS/NW Pacific to the TIO warming is consistent with modeling studies of Watanabe and Jin (2002) and Annamalai et al. (2005a). Wind anomalies are dominated by a C-shaped pattern, northeasterly north and southwesterly south of the equator. It is somewhat surprising that the symmetric SST anomalies force an antisymmetric atmospheric response, a nonlinearity likely due to the southward displacement of the Indian Ocean ITCZ during boreal winter and spring. Convective response to SST changes is likely larger in the ITCZ south of the equator than over the cold and dry NIO. To assess the effect of the direct Pacific SST forcing, we have carried out another atmospheric GCM run with SST anomalies limited to the tropical Pacific (20°S–20°N), specified to be the MAM(1) regression pattern referenced to the NDJ(0) Niño-3.4 SST. In this tropical Pacific run, the atmospheric response is nearly symmetric about the equator and features easterly wind anomalies near the equator (not shown). Thus, the antisymmetric pattern of atmospheric anomalies observed during March–April(1) is forced internally by TIO SST anomalies, the basin-wide warming in particular. To be reported elsewhere, a comparison of atmospheric GCM simulations forced with observed SST over the global ocean and TIO confirms this conclusion.

The SIO run reproduces the spatial pattern of atmospheric anomalies in the TIO run (Fig. 11c), albeit with reduced magnitude, indicating that the SIO warming is the major forcing for the antisymmetric pattern. The additional SWIO run confirms that the SWIO warming is important for the antisymmetric wind pattern (Fig. 11e). The SWIO warming in turn is largely due to the deepening of the thermocline associated with the ocean

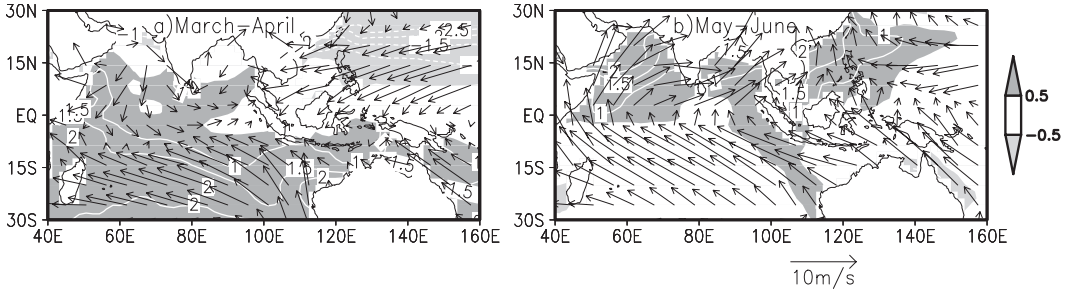

FIG. 10. Climatology of wind and SST expressed as deviations from the annual mean: (a) March–April and (b) May–June.

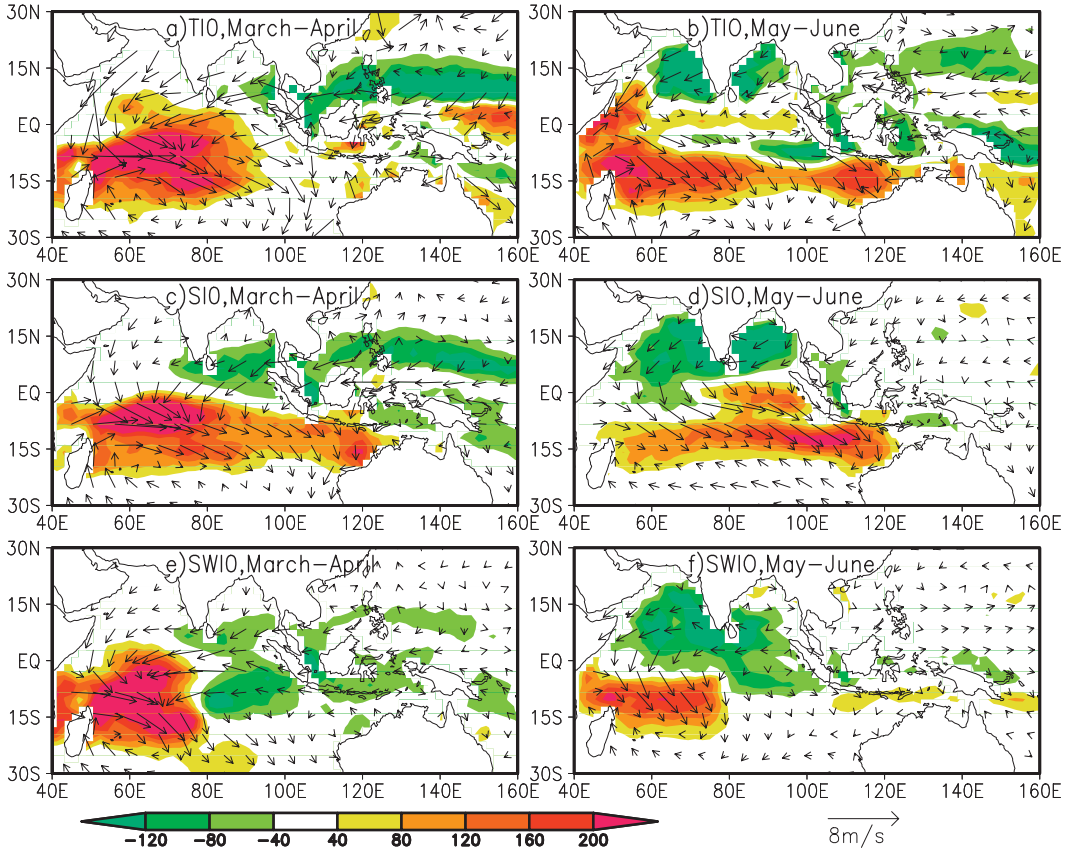

FIG. 11. Atmospheric model response to a 1°C SST warming. Precipitation (mm month^{-1}) and wind velocity (m s^{-1}) anomalies in (top) the TIO, (middle) SIO, and (bottom) SWIO runs during (left) March–April and (right) May–June.

Rossby waves. Both oceanic and atmospheric conditions are favorable for the ocean Rossby waves to affect the atmosphere during boreal spring: the seasonal thermocline shoaling associated with the annual Rossby wave (Fig. 6b) enables a strong thermocline feedback on SST while the southward-displaced ITCZ allows a strong precipitation and hence wind response. The importance of ocean Rossby waves for the antisymmetric atmospheric anomalies is hinted by experiments using an atmospheric GCM forced by observed SST anomalies over the tropical Pacific but coupled with an ocean mixed layer model elsewhere. In such a model, the antisymmetric atmospheric pattern is absent over the TIO during the spring following El Niño (Lau and Nath 2003, their Fig. 3b), presumably because of the lack of ocean Rossby wave dynamics.

Atmospheric GCM results are similar during May–June(1), reproducing successfully observed atmospheric anomalies (cf. Figs. 8b,h). The antisymmetric atmospheric pattern over the TIO is largely due to the SWIO warming (Figs. 11b,f). In particular, the resultant northeasterly wind anomalies north of the equator force the second warming of the NIO via AtF-L following the southwest monsoon onset (Fig. 8e). The comparison of the TIO and SIO runs indicates that the NIO warming helps extend the easterly wind anomalies eastward into the SCS and NW Pacific. These easterly anomalies cause the subsequent warming over the SCS and NW Pacific as the mean winds turn westerly.

c. *Persistence through summer*

In July–August(1), the SWIO SST warming is still visible but weakens and shrinks in area as the ocean Rossby wave decays (Fig. 8c). Positive SST anomalies remain strong north of the equator from the NIO to the NW Pacific. Upwelling changes help amplify these anomalies in the west Arabian Sea (Izumo et al. 2008) and SCS (Xie et al. 2003). There are weak positive precipitation anomalies over the TIO (Fig. 8i). Wind anomalies are weak over much of the TIO. Northeasterly wind anomalies retreat to the east over the Bay of Bengal, SCS, and NW Pacific as part of an anticyclonic circulation centered in the subtropical NW Pacific, where rainfall decreases.

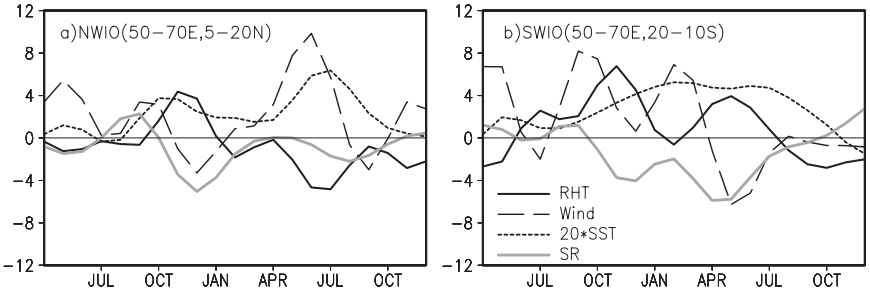

FIG. 12. Heat budget terms (W m^{-2}) in (a) the northwest and (b) southwest IO. Abbreviations: RHT [latent heat flux anomalies (LHF) due to changes in relative humidity and air–sea temperature difference], wind (wind effect on LHF), and SR (solar radiation).

The TIO warming and NW Pacific anticyclone are the most robust anomalies in the ocean and atmosphere, respectively, during the summer following El Niño, suggesting that the former is forcing the latter (Yang et al. 2007). Xie et al. (2009) propose a Kelvin wave–induced Ekman divergence mechanism for the TIO to affect the subtropical NW Pacific. The TIO warming forces a warm baroclinic Kelvin wave that propagates into the western Pacific. The resultant surface divergence over the subtropical NW Pacific triggers the suppression of convection there, leading eventually to the development of an anomalous anticyclone.

Thus, from a meteorological point of view, the NW Pacific anticyclone is forced by the TIO warming. From an oceanographic point of view, on the other hand, the warming north of the equator, from the Bay of Bengal to the NW Pacific, is sustained by the northeasterly wind anomalies of the NW Pacific anticyclone via AtF-L (Fig. 8f). This circular argument suggests ocean–atmosphere interactionbetween the northern SST warming and the NW Pacific atmospheric anticyclone during July–August(1). We plan to pursue this possibility in future studies.

5. Discussion

a. Possible air temperature and relative humidity effects

During El Niño, air temperature in the free troposphere increases over the tropics (Yulaeva and Wallace 1994). Through deep convection, this tropospheric temperature warming is mixed into the atmospheric boundary layer, raising SST via turbulent heat flux. Chiang and Sobel (2002) propose this mechanism for the warming of the tropical Atlantic and Indian Oceans during El Niño, a hypothesis gaining support from the observational analysis of Chikamoto and Tanimoto (2005) for the tropical North Atlantic Ocean in MAM(1) following El Niño. To test this hypothesis for the TIO, we further decompose the AtF-L by linearizing Eq. (1) with regard to wind speed, air–sea temperature difference, and relative humidity. The wind change effect almost always dominates, but the air–sea temperature difference and relative humidity effects can be important in certain regions and periods, as identified below.

In the northwestern TIO (5°–20°N, 50°–70°E), the air–sea temperature difference and relative humidity contributions are positive during the 3–4 months centered in November–December(0) while both the wind and solar radiation effects are negative (Fig. 12a). In the subtropical SWIO (20°–10°S, 50°–70°E), the air–sea temperature difference and relative humidity effects are positive during July(0)–January(1), especially during October(0)–December(0) when the wind effect begins to decrease (Fig. 12b), a result consistent with Chiodi and Harrison (2007). It is somewhat puzzling that both cases take place in the developing/mature phase of El Niño when the tropospheric warming is not yet fully developed over the TIO. Over the subtropical SWIO, the air–sea temperature difference and relative humidity effects become significant again during March(1)–June(1) (Fig. 12b).

b. Individual case

By some measures, the 1997/98 event is the largest El Niño on the instrumental record. Figure 13 shows ocean–atmospheric anomalies during the decay phase of this El Niño event. The 1998 anomalies are larger by a factor of 2–3 than regression coefficients discussed earlier but otherwise similar in spatial pattern. In March–April 1998, the meridional asymmetric pattern appears over the TIO in surface winds and solar radiation. This pattern persists through May–June, helping to spread the SST warming to the entire NIO. The asymmetric atmospheric pattern, with a cyclonic circulation over the SWIO and northeasterly anomalies north of the equator from the NIO to NW Pacific, remains discernible even during July–August 1998 possibly because of very large

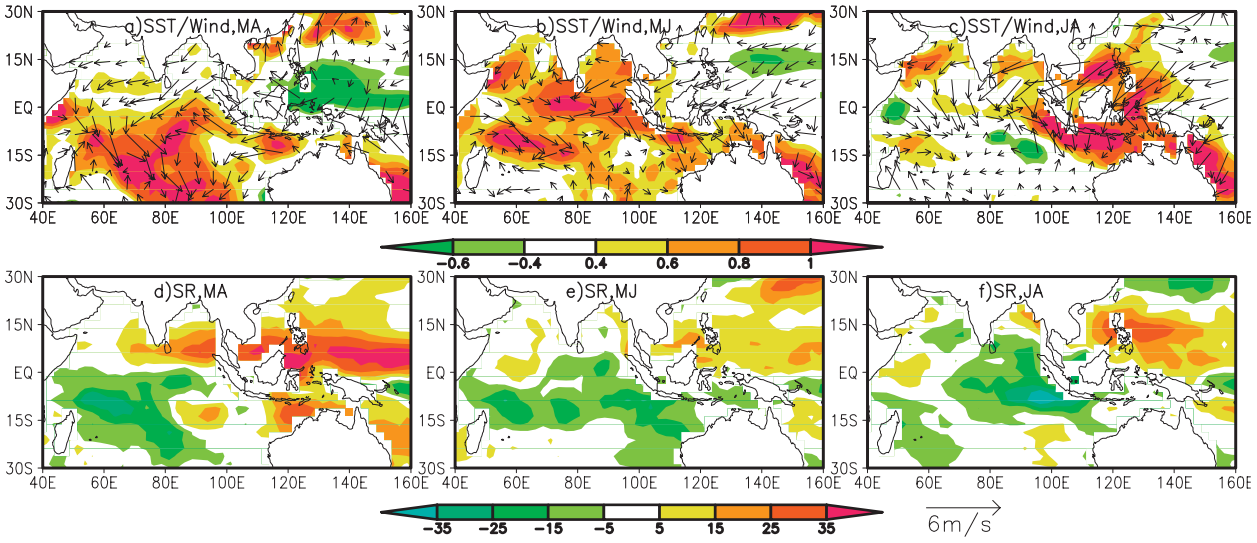

FIG. 13. As in Fig. 8, but for SST (top) wind velocity and (bottom) solar radiation anomalies during the 1998 warming event.

SST forcing (~1°C). A strong SST warming takes place off Java and Sumatra, a feature associated with a strong deepening of the thermocline but absent in the regression map.

6. Summary

We have investigated the mechanisms that give rise to and sustain the TIO warming after El Niño by using atmospheric reanalyses, satellite measurements, and ocean and atmospheric GCM simulations. Since El Niño is strongly phase locked onto the seasonal cycle, our main analysis is based on regression and correlation stratified in calendar month and referenced to the NDJ(0) Niño-3.4 SST index. The TIO warming displays considerable regional variations. While the SWIO features a sustained warming from November(0) to August(1), the NIO and SCS warming displays two peaks in November–December(0) and June–August(1), respectively, with the second peak larger in magnitude. Our mixed layer heat budget indicates that surface heat flux is the dominant mechanism for the El Niño–induced warming except over the south TIO. Specifically, solar radiation contributes to the warming in the southeast TIO and the first warming in the SCS, consistent with previous studies (Klein et al. 1999; Tokinaga and Tanimoto 2004). In the NIO and SCS, atmospheric forcing via LHF is identified as the major cause of the second warming. The weakened southwest monsoon reduces LHF and prolongs the SST warming to JJA(1) in the Bay of Bengal and SCS.

The second warming in the summer NIO and SCS is peculiar in that it takes place while El Niño begins its rapid decay. Our recent study indicates that the NIO warming causes robust atmospheric anomalies over the Indo-western Pacific during the summer following El Niño (Xie et al. 2009), motivating us here to take a close look into what causes this summer NIO warming. Our results reveal that internal air–sea interaction within the TIO is key to the long persistence of the SST warming, as summarized in the following conceptual model.

During an El Niño/IOD event, Walker circulation adjustments feature easterly wind anomalies in the equatorial IO with anticyclonic curls in the southeast TIO, forcing a downwelling Rossby wave traveling westward along 10°S. As it propagates into the SWIO thermocline dome, the downwelling Rossby wave lowers the thermocline, reduces upwelling, and raises SST (Xie et al. 2002; Huang and Kinter 2002). During MAM(1), the Rossby wave–induced warming over the SWIO intensifies atmospheric deep convection and excites a cyclonic surface circulation to the south.

Besides these local atmospheric anomalies, the SWIO warming induces a basin-wide antisymmetric pattern in the atmosphere during spring and early summer, with northeasterly (northwesterly) wind anomalies north (south) of the equator. Atmospheric GCM experiments confirm this SWIO forcing hypothesis. During late winter to early spring, this antisymmetric atmospheric pattern interacts with the TIO via the positive WES feedback: the anomalous winds intensify the prevailing northeasterly monsoon north and weaken the southeast trades south of the equator, acting to establish a southward SST gradient (Kawamura et al. 2001; Wu et al. 2008). The antisymmetric wind anomaly pattern persists

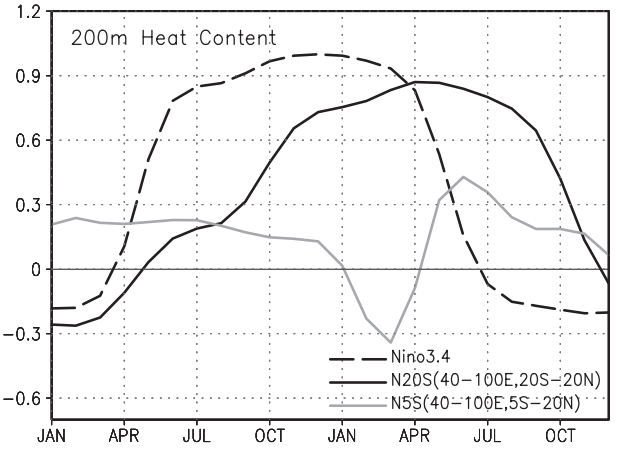

FIG. 14. Correlation of the upper 200-m heat content with the NDJ(0) Niño-3.4 index.

through May–June(1). As the prevailing winds turn into southwesterly following the summer monsoon onset in May, the northeasterly anomalies act to reduce the southwest monsoon and warm the ocean, giving rise the pronounced second warming over the NIO and SCS. Consistent with the double-peak warming, the AtF-L component features two peaks during and slightly before the SST warming over the NIO and SCS.

At the height of summer following El Niño [July–August(1)], the NIO, SCS, and NW Pacific remain warm while the northeasterly anomalies retreat into the Bay of Bengal and SCS as part of a robust anticyclone centered in the NW Pacific. To the extent that the NIO warming sustains the NW Pacific anticyclone (Yang et al. 2007; Xie et al. 2009), there is a two-way interaction between them, a process that needs further study.

Figure 14 clarifies the TIO capacitor effect and identifies where the heat storage change takes place. While temperature changes are confined in the thin ocean mixed layer north of 5°S, the memory of El Niño is stored in a much deeper layer in the upper thermocline to the south in the form of slowly propagating Rossby wave. Our results confirm the conclusion in the literature that surface heat flux changes are the dominant mechanism for the TIO warming that follows the El Niño peak (Klein et al. 1999; Alexander et al. 2002; Lau and Nath 2003; Tokinaga and Tanimoto 2004; Shinoda et al. 2004), except for the tropical SWIO. Our study extends the previous research, which is based on local heat budget analysis, by identifying a basin-scale, antisymmetric atmospheric pattern as what gives rise to surface heat flux changes and the second NIO warming. We further show that this atmospheric pattern is induced by the SWIO ocean Rossby wave and results from their mutual interaction. Thus, the ocean dynamics plays a much more important role than previously thought, now extending to the persistence and capacitor effect of the TIO warming. This recognition of the ocean dynamic effect has important implications for climate prediction, calling for improved monitoring and modeling of SWIO Rossby waves.

Acknowledgments. We wish to thank H. Sasaki and the OFES group for providing the ocean hindcast, and APDRC for maintaining the local database. This work is supported by the Knowledge Innovation Project of the Chinese Academy of Sciences (KZCX2-YW-BR-04, KZCX2-YW-220, and LYQY200807), the U.S. National Science Foundation, the Japan Agency for Marine-Earth Science and Technology, and the Natural Science Foundation of China (40876007, 40775051, and U0733002).

REFERENCES

Alexander, M. A., I. Bladé, M. Newman, J. R. Lanzante, N.-C. Lau, and J. D. Scott, 2002: The atmospheric bridge: The influence of ENSO teleconnections on air–sea interaction over the global oceans. *J. Climate,* **15,** 2205–2231.

Annamalai, H., and R. Murtugudde, 2004: Role of the Indian Ocean in regional climate variability. *Earth's Climate: The Ocean–Atmosphere Interaction, Geophys. Monogr.,* Vol. 147, Amer. Geophys. Union, 213–246.

——, P. Liu, and S.-P. Xie, 2005a: Southwest Indian Ocean SST variability: Its local effect and remote influence on Asian monsoons. *J. Climate,* **18,** 4150–4167.

——, S. P. Xie, J. P. McCreary, and R. Murtugudde, 2005b: Impact of Indian Ocean sea surface temperature on developing El Niño. *J. Climate,* **18,** 302–319.

Behera, S. K., and T. Yamagata, 2001: Subtropical SST dipole events in the southern Indian Ocean. *Geophys. Res. Lett.,* **28,** 327–330.

——, P. S. Salvekar, and T. Yamagata, 2000: Simulation of interannual SST variability in the tropical Indian Ocean. *J. Climate,* **13,** 3487–3499.

Chang, P., and Coauthors, 2006: Climate fluctuations of tropical coupled system— The role of ocean dynamics. *J. Climate,* **19,** 5122–5174.

Chen, J.-M., T. Li, and C.-F. Shih, 2007: Fall persistence barrier of sea surface temperature in the South China Sea associated with ENSO. *J. Climate,* **20,** 158–172.

Chiang, J. C. H., and A. H. Sobel, 2002: Tropical tropospheric temperature variations caused by ENSO and their influence on the remote tropical climate. *J. Climate,* **15,** 2616–2631.

Chikamoto, Y., and Y. Tanimoto, 2005: Role of specific humidity anomalies in Caribbean SST response to ENSO. *J. Meteor. Soc. Japan,* **83,** 959–975.

Chiodi, A. M., and D. E. Harrison, 2007: Mechanisms of summertime subtropical southern Indian Ocean sea surface temperature variability: On the importance of humidity anomalies and the meridional advection of water vapor. *J. Climate,* **20,** 4835–4852.

Chowdary, J. S., C. Gnanaseelan, and S. P. Xie, 2009: Westward propagation of barrier layer formation in the 2006-07 Rossby

wave event over the tropical southwest Indian Ocean. *Geophys. Res. Lett.,* **36,** L04607, doi:10.1029/2008GL036642.

Deser, C., A. S. Phillips, and J. W. Hurrell, 2004: Pacific interdecadal climate variability: Linkages between the tropics and the North Pacific during boreal winter since 1900. *J. Climate,* **17,** 3109–3124.

de Szoeke, S. P., S.-P. Xie, T. Miyama, K. J. Richards, and R. J. O. Small, 2007: What maintains the SST front north of the eastern Pacific equatorial cold tongue? *J. Climate,* **20,** 2500–2514.

Dommenget, D., V. Semenov, and M. Latif, 2006: Impacts of the tropical Indian and Atlantic Oceans on ENSO. *Geophys. Res. Lett.,* **33,** L11701, doi:10.1029/2006GL025871.

Du, Y., and S.-P. Xie, 2008: Role of atmospheric adjustments in the tropical Indian Ocean warming during the 20th century in climate models. *Geophys. Res. Lett.,* **35,** L08712, doi:10.1029/2008GL033631.

——, T. Qu, and G. Meyers, 2008: Interannual variability of the sea surface temperature off Java and Sumatra in a global GCM. *J. Climate,* **21,** 2451–2465.

Han, W., D. Yuan, W. T. Liu, and D. J. Halkides, 2007: Intraseasonal variability of Indian Ocean sea surface temperature during boreal winter: Madden–Julian Oscillation versus submonthly forcing and processes. *J. Geophys. Res.,* **112,** C04001, doi:10.1029/2006JC003791.

Huang, B., and J. L. Kinter III, 2002: Interannual variability in the tropical Indian Ocean. *J. Geophys. Res.,* **107,** 3199, doi:10.1029/2001JC001278.

Izumo, T., C. de Boyer Montégut, J.-J. Luo, S. K. Behera, S. Masson, and T. Yamagata, 2008: The role of the western Arabian Sea upwelling in Indian monsoon rainfall variability. *J. Climate,* **21,** 5603–5623.

Kanamitsu, M., W. Ebisuzaki, J. Woollen, S.-K. Yang, J. J. Hnilo, M. Fiorino, and G. L. Potter, 2002: NCEP–DOE AMIP-II reanalysis (R-2). *Bull. Amer. Meteor. Soc.,* **83,** 1631–1643.

Kawamura, R., T. Matsuura, and S. Iizuka, 2001: Role of equatorially asymmetric sea surface temperature anomalies in the Indian Ocean in the Asian summer monsoon and El Niño–Southern Oscillation coupling. *J. Geophys. Res.,* **106,** 4681–4693.

Klein, S. A., B. J. Soden, and N.-C. Lau, 1999: Remote sea surface temperature variations during ENSO: Evidence for a tropical atmospheric bridge. *J. Climate,* **12,** 917–932.

Kug, J.-S., and I.-S. Kang, 2006: Interactive feedback between ENSO and the Indian Ocean. *J. Climate,* **19,** 1784–1801.

Lau, N.-C., and M. J. Nath, 2000: Impact of ENSO on the variability of the Asian–Australian monsoons as simulated in GCM experiments. *J. Climate,* **13,** 4287–4309.

——, and ——, 2003: Atmosphere–ocean variations in the Indo-Pacific sector during ENSO episodes. *J. Climate,* **16,** 3–20.

Liu, Q., X. Jiang, S.-P. Xie, and W. T. Liu, 2004: A gap in the Indo-Pacific warm pool over the South China Sea in boreal winter: Seasonal development and interannual variability. *J. Geophys. Res.,* **109,** C07012, doi:10.1029/2003JC002179.

Masumoto, Y., and G. Meyers, 1998: Forced Rossby waves in the southern tropical Indian Ocean. *J. Geophys. Res.,* **103,** 27 589–27 602.

——, and Coauthors, 2004: A fifty-year eddy-resolving simulation of the world ocean—Preliminary outcomes of OFES (OGCM for the Earth Simulator). *J. Earth Simulator,* **1,** 35–56.

Murtugudde, R., J. P. McCreary Jr., and A. J. Busalacchi, 2000: Oceanic processes associated with anomalous events in the Indian Ocean with relevance to 1997–1998. *J. Geophys. Res.,* **105,** 3295–3306.

Périgaud, C., and P. Delecluse, 1992: Annual sea level variations in the southern tropical Indian Ocean from Geosat and shallow-water simulations. *J. Geophys. Res.,* **97,** 20 169–20 178.

Rao, S. A., and S. K. Behera, 2005: Subsurface influence on SST in the tropical Indian Ocean: Structure and interannual variability. *Dyn. Atmos. Oceans,* **39,** 103–135.

Roeckner, E., and Coauthors, 2003: The atmospheric general circulation model ECHAM5. Part I: Model description. Max-Planck-Institut für Meteorologie Tech. Rep. 349, 140 pp.

Saji, N. H., B. N. Goswami, P. N. Vinayachandran, and T. Yamagata, 1999: A dipole mode in the tropical Indian Ocean. *Nature,* **401,** 360–363.

Sasaki, H., M. Nonaka, Y. Masumoto, Y. Sasai, H. Uehara, and H. Sakuma, 2008: An eddy-resolving hindcast simulation of the quasiglobal ocean from 1950 to 2003 on the Earth Simulator. *High Resolution Numerical Modelling of the Atmosphere and Ocean*, W. Ohfuchi and K. Hamilton, Eds., Springer, 157–185.

Schiffer, R. A., and W. B. Rossow, 1985: ISCCP global radiance data set: A new resource for climate research. *Bull. Amer. Meteor. Soc.,* **66,** 1498–1505.

Schott, F. A., S.-P. Xie, and J. P. McCreary Jr., 2009: Indian Ocean circulation and climate variability. *Rev. Geophys.,* **47,** RG1002, doi:10.1029/2007RG000245.

Shinoda, T., M. A. Alexander, and H. H. Hendon, 2004: Remote response of the Indian Ocean to interannual SST variations in the tropical Pacific. *J. Climate,* **17,** 362–372.

Tokinaga, H., and Y. Tanimoto, 2004: Seasonal transition of SST anomalies in the tropical Indian Ocean during El Niño and Indian Ocean dipole years. *J. Meteor. Soc. Japan,* **82,** 1007–1018.

Wang, C., W. Wang, D. Wang, and Q. Wang, 2006: Interannual variability of the South China Sea associated with El Niño. *J. Geophys. Res.,* **111,** C03023, doi:10.1029/2005JC003333.

Wang, L., C. J. Koblinsky, and S. Howden, 2001: Annual Rossby wave in the southern Indian Ocean: Why does it ''appear'' to break down in the middle ocean? *J. Phys. Oceanogr.,* **31,** 54–74.

Watanabe, M., and F.-F. Jin, 2002: Role of Indian Ocean warming in the development of Philippine Sea anticyclone during ENSO. *Geophys. Res. Lett.,* **29,** 1478, doi:10.1029/2001GL014318.

Weare, B. C., 1979: A statistical study of the relationships between ocean surface temperatures and the Indian monsoon. *J. Atmos. Sci.,* **36,** 2279–2291.

Webster, P. J., A. M. Moore, J. P. Loschnigg, and R. R. Leben, 1999: Coupled ocean–atmosphere dynamics in the Indian Ocean during 1997–98. *Nature,* **401,** 356–360.

Wu, R., and B. P. Kirtman, 2004: Understanding the impacts of the Indian Ocean on ENSO variability in a coupled GCM. *J. Climate,* **17,** 4019–4031.

——, ——, and V. Krishnamurthy, 2008: An asymmetric mode of tropical Indian Ocean rainfall variability in boreal spring. *J. Geophys. Res.,* **113,** D05104, doi:10.1029/2007JD009316.

Xie, P., and P. A. Arkin, 1997: Global precipitation: A 17-year monthly analysis based on gauge observations, satellite estimates, and numerical model outputs. *Bull. Amer. Meteor. Soc.,* **78,** 2539–2558.

Xie, S.-P., and S. G. H. Philander, 1994: A coupled ocean-atmosphere model of relevance to the ITCZ in the eastern Pacific. *Tellus,* **46A,** 340–350.

——, H. Annamalai, F. Schott, and J. P. McCreary Jr., 2002: Origin and predictability of South Indian Ocean climate variability. *J. Climate,* **15,** 864–878.

——, Q. Xie, D. X. Wang, and W. T. Liu, 2003: Summer upwelling in the South China Sea and its role in regional climate variations. *J. Geophys. Res.,* **108,** 3261, doi:10.1029/2003JC001867.

——, K. Hu, J. Hafner, Y. Du, G. Huang, and H. Tokinaga, 2009: Indian Ocean capacitor effect on Indo-western Pacific climate during the summer following El Niño. *J. Climate,* **22,** 730–747.

Yamagata, T., S. K. Behera, J. J. Luo, S. Masson, M. R. Jury, and S. A. Rao, 2004: Coupled ocean–atmosphere variability in the tropical Indian Ocean. *Earth's Climate: The Ocean–Atmosphere Interaction, Geophys. Monogr.,* Vol. 147, Amer. Geophys. Union, 189–211.

Yang, J., Q. Liu, S.-P. Xie, Z. Liu, and L. Wu, 2007: Impact of the Indian Ocean SST basin mode on the Asian summer monsoon. *Geophys. Res. Lett.,* **34,** L02708, doi:10.1029/2006GL028571.

Yokoi, T., T. Tozuka, and T. Yamagata, 2008: Seasonal variation of the Seychelles Dome. *J. Climate,* **21,** 3740–3754.

Yu, L., and M. M. Rienecker, 1999: Mechanisms for the Indian Ocean warming during the 1997–98 El Niño. *Geophys. Res. Lett.,* **26,** 735–738.

Yu, W., B. Xiang, L. Liu, and N. Liu, 2005: Understanding the origins of interannual thermocline variations in the tropical Indian Ocean. *Geophys. Res. Lett.,* **32,** L24706, doi:10.1029/2005GL024327.

Yulaeva, E., and J. M. Wallace, 1994: The signature of ENSO in global temperature and precipitation fields derived from the microwave sounding unit. *J. Climate,* **7,** 1719–1736.